Article

Influence of Heat Treatment on Precipitate and Microstructure of 38CrMoAl Steel

Guofang Xu , Shiheng Liang , Bo Chen , Jiangtao Chen , Yabing Zhang , Xiaotan Zuo , Zihan Li , Bo Song * , Wei Liu *

Posted Date: 27 June 2025

doi: 10.20944/preprints202506.2219.v1

Keywords: precipitate; microstructure; hot ductility; 38CrMoAl steel

Article

Influence of Heat Treatment on Precipitate and Microstructure of 38CrMoAl Steel

Guofang Xu [1], Shiheng Liang [1], Bo Chen [1], Jiangtao Chen [2], Yabing Zhang [2], Xiaotan Zuo [2], Zihan Li [3], Bo Song [1,*] and Wei Liu [1,*]

[1] School of Metallurgical and Ecological Engineering, University of Science and Technology Beijing, Beijing, China
[2] Wuhu Xinxing Ductile Pipe Co., Ltd., Wuhu, 241002, Anhui, China
[3] HBIS Material Technology Research Institute, Shijiazhuang 052160, Hebei, China
* Correspondence: songbo@metall.ustb.edu.cn (B.S.); liuwei@ustb.edu.cn (W.L.)

Abstract

To address the central cracking problem in continuous casting slabs of 38CrMoAl steel, high-temperature tensile tests were performed using a Gleeble-3800 thermal simulator to characterize the hot ductility of the steel within 600 – 1200 °C. Phase transformation behavior was computationally analyzed via Thermo-Calc software, while microstructure, fracture morphology, and precipitate characteristics were systematically investigated using metallographic microscope(MM), field emission scanning electron microscope(FE-SEM), and transmission electron microscopy(TEM). Additionally, the effects of different holding times and cooling rates on the microstructure and precipitates of 38CrMoAl steel were also studied. The results show that the third brittle temperature range of 38CrMoAl steel is 645 – 1009 °C, and the fracture mechanisms can be classified into three types: (I) In the α single-phase region, the thickness of intergranular proeutectoid ferrite increases with rising temperature, leading to reduced hot ductility; (II) In the γ single-phase region, the average size of precipitates increases while the number density decreases with increasing temperature, thereby improving hot ductility; (III) In the $\alpha + \gamma$ two-phase region, the precipitation of proeutectoid ferrite promotes crack propagation, and the dense distribution of precipitates at grain boundaries causes stress concentration, further deteriorating hot ductility. Heat treatment experiments indicate that under water cooling, air cooling, and furnace cooling conditions, the microstructures of the specimen transform as follows: martensite + proeutectoid ferrite → bainite + ferrite → ferrite; the average size of precipitates first decreases, then increases, and finally decreases again with increasing holding time, while the number density exhibits the opposite trend. Therefore, when the holding time is the same, reducing the cooling rate can increase the average size of precipitates and decrease their number density, thereby improving the hot ductility of 38CrMoAl steel.

Keywords: precipitate; microstructure; hot ductility; 38CrMoAl steel

---

1. Introduction

According to Chinese standards (GB/T 3077–2015) [1], 38CrMoAl steel is an alloy structural steel with an aluminum content as high as 1 wt%, which is mainly used for gears [2], hydraulic plungers [3], carrier aircraft [4]. Due to its high Al content, this steel tends to cause nozzle clogging during continuous casting. Meanwhile, casting billets are prone to metallurgical defects like cracks and component segregation [5]. The industrial production route for Φ600 mm 38CrMoAl steel at a domestic factory is as follows: Linz-Donawitz(LD) → Ladle furnace(LF) → RH-vacuum degassing(RH) → Continue Cast(CC) → Rapid Forging → Diameter Forging. However, it is found in production that the cooled continuous casting billets have central cracks, which seriously affect the quality of the billets and subsequent processing.

The initiation and propagation of cracks in continuous casting billets are intimately linked to the high-temperature mechanical properties of steel. Generally, cracks are related to the hot ductility of steel [**6–13**], which influences the fatigue properties [14] and internal quality [**15,16**] of steel. For high-Al steel grades, existing researches on cracking mechanisms primarily focuses on non-metallic inclusions [**17,18**], strain rate and cooling rate [**10,18–20**], micro-alloying elements [**8,20**] and harmful elements (S, N, P) [**9,20,21**]. In other steel types, such as API X60 micro-alloyed steel, the hot ductility is related to the austenite grain size, the size and volume fraction of precipitated phases [22]; for alloy structural steels like 2.25Cr-1Mo, the hot ductility is associated with precipitated phases and ferrite [**23–25**]. The hot ductility of steel reveals its deformation behavior and fracture mechanism at high temperatures, providing a theoretical basis for predicting cracks in continuous casting billets, reducing processing defects, and optimizing processes.

However, systematic data about the microstructure and precipitates near the fracture on the hot ductility of industrial-grade 38CrMoAl continuous casting billets remain scarce. To address this gap and improve the cracks, this study investigates 38CrMoAl steels from continuous casting billets using a Gleeble-3800 testing machine to characterize their high-temperature mechanical properties across 600-1200 °C. The aim is to provide guidance for the industrial production of 38CrMoAl continuous casting billets with high yield. Meanwhile, the effects of different holding times and cooling rates on the precipitates and microstructure of 38CrMoAl steel were investigated.

2. Experimental Materials and Methods

2.1. Experimental Materials

Experimental samples were extracted from on-site continuous casting billets. The chemical composition of the 38CrMoAl steel continuous cast billets is shown in Table 1. The schematic diagram of the sample is shown in Figure 1.

Table 1. The chemical composition of 38CrMoAl steel (mass fraction，wt%).

C	Si	Mn	P	S	O	N	Ti	Cr	Mo	Al	Fe
0.39	0.31	0.42	0.0130	0.0010	0.0005	0.0031	0.0127	1.53	0.10	0.85	Bal.

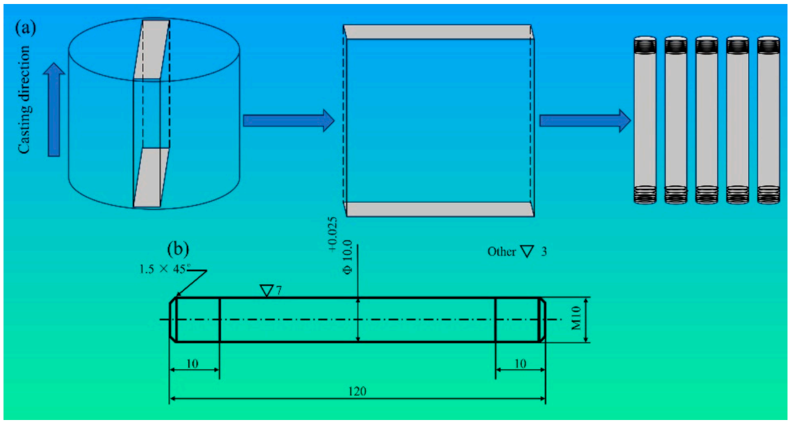

Figure 1. Diagram of the Sample: (a) diagrams of sampling schematic; (b) tensile specimen.

2.2. Experimental Methods

(1) High-temperature Tensile Test

The thermal simulation test schedule of hot tensile tests is shown in Figure 2. Specimens were heated to 1300 °C at a rate of 10 °C/s and subjected to a 300-second, followed by a controlled cooling at 3 °C/s to the target temperature range of 600 – 1200 °C. After a 60-second isothermal hold at each test temperature, tensile testing with Gleeble-3800 (DSI, USA) was performed at a constant strain rate of $10^{-3}s^{-1}$ *[18,24]*. Upon fracture, specimens were immediately water-quenched to retain the high-temperature fracture morphology and microstructural features *[*26].

The reduction of area (RA) and tensile strength (σb) were calculated using formula (1) and (2):

$$RA=\frac{D_0^2-D_1^2}{D_0^2}\times 100\% \tag{1}$$

$$\sigma_b=\frac{4F_{max}}{\pi D_0^2} \tag{2}$$

where D_0 is the original diameter of the sample, which is 10 mm; and D_1 is the diameter of the sample after fracture (mm); F_{max} is the maximum tensile force endured by the sample during the tensile process (N); D_0 is the original diameter of the sample, which is 10 mm; σ_b is the tensile strength of the sample (MPa).

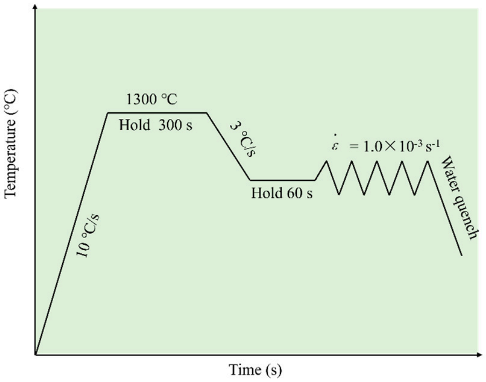

Figure 2. Thermal simulation test schedule of hot tensile tests.

(2) Heat Treatment Experiment

The high-temperature molybdenum wire furnace was heated to 950°C. Metallographic specimens (10 mm × 10 mm × 10 mm) were placed in an alumina crucible and subjected to isothermal holding for 20 min, 40 min, 60 min, 80 min, and 100 min respectively. After each holding period, partial specimens were rapidly quenched via water cooling and air cooling, while the remaining specimens were furnace cooling. Subsequently, the specimens were subjected to precipitated and microstructure analysis. The structural schematic of the high-temperature molybdenum wire furnace is presented in **Error! Reference source not found.**.

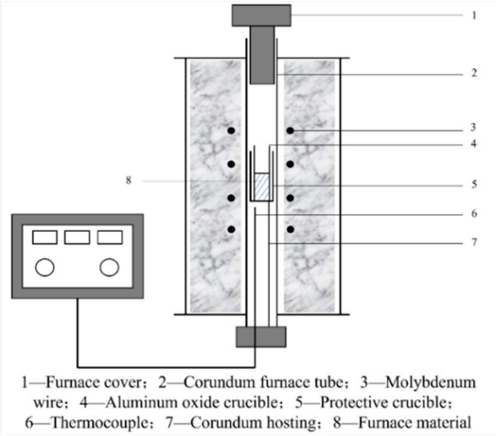

Figure 3. Structure diagram of high-temperature molybdenum wire furnace.

(3) Fracture Morphology, Microstructure, Grain Size and Precipitated Phases Characterization

The fracture morphology was observed under a field emission scanning electron microscope (FE-SEM, GeminiSEM300). Microstructural observations of both fracture and heat-treated samples were conducted via a metallographic microscope (MM). The grain sizes near the fracture were performed Image-Pro Plus software. And Thermo-Calc software, combined with the TCFE v8.1 thermodynamic database, was employed to simulate phase transformations in 38CrMoAl steel. Transmission electron microscopy (TEM, JEOL JEM-2010) operated at 200 kV, coupled with energy dispersive spectroscopy (EDS), was used to characterize the morphology, size of precipitates and chemical composition.

3. Results and Discussion

3.1. Hot Ductility

RA is used to measure the hot ductility of the sample [12,13,19,24,27,28], with its calculation defined by formula (1). In this study, RA = 40% is taken as the critical threshold of the crack-sensitive zone during the continuous casting and straightening process [17,27,29]. When RA < 40%, it indicates that the steel grade is prone to cracking during continuous casting, and the corresponding temperature range is regarded as the brittle zone.

Figure 4 shows the hot ductility curve across varying temperatures. Notably, within the test temperature range, no high-temperature brittle zone or the first brittle zone was detected. Given that the applied strain rate ($1.0 \times 10^{-3}s^{-1}$) was lower than the threshold (1.0×10^{-2} s^{-1}) for the second brittle temperature zone's formation *[*13], this experimental condition excluded the occurrence of the second brittle zone. Based on the critical threshold of RA = 40% for the crack-sensitive zone during continuous casting and straightening, the variation of the RA value with temperature can be divided into three categories: (I) Low-Temperature Ductility Zone (600 °C): The RA value at 600°C is approximately 57.5%, indicating favorable ductility at lower temperatures. (II) Medium-Temperature Brittle Zone (645 – 1009 °C): The ductility trough spans 645 - 1009 °C, with corresponding RA values ≤40%. The temperature range is identified as the primary brittle zone where cracking susceptibility is highest during continuous casting. (III) High-Temperature Ductility Zone (1050 – 1200 °C): Within this interval, the RA value exhibits a non-monotonic trend: increasing first, then decreasing, and increasing again with rising temperature. All RA values exceed 40%, with a peak of ~83.5% observed at 1100 °C.

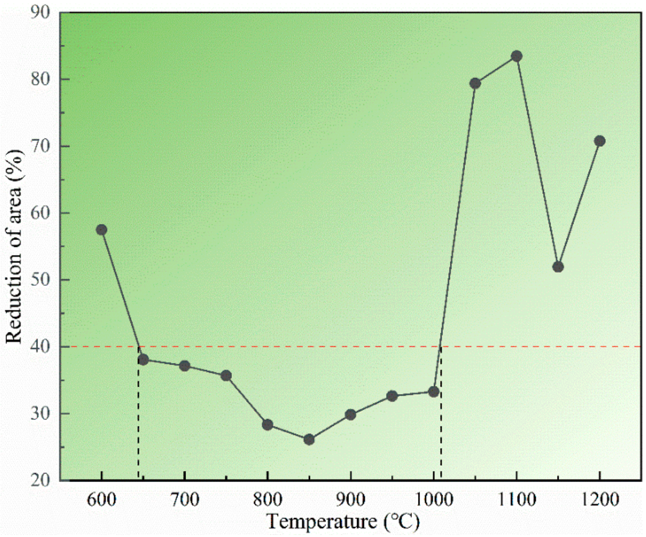

Figure 4. Reduction of area of 38CrMoAl steel specimens.

3.2. Tensile Strength

Figure 5 demonstrates that the tensile strength of 38CrMoAl steel exhibits a rapid decline in the 600 – 950 °C temperature range, followed by a slower decrease from 950 – 1200 °C. Notably, the peak tensile strength of ~267.5 MPa occurs at 600 °C, while the minimum value of ~13.9 MPa is recorded at 1200 °C.

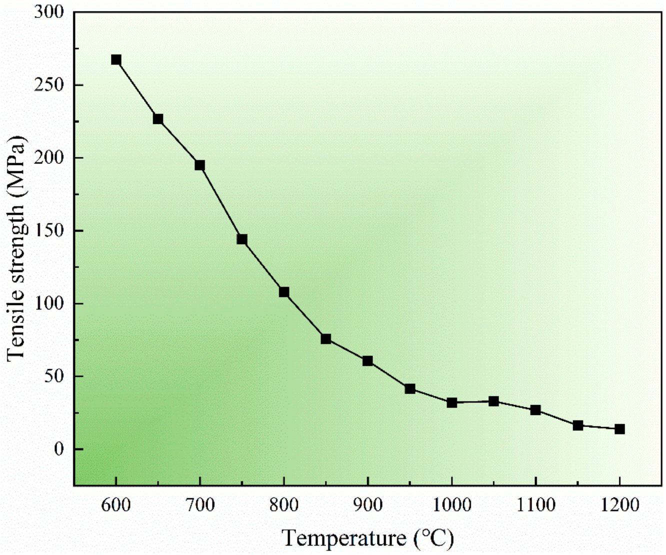

Figure 5. Tensile strength of 38CrMoAl steel specimens.

3.3. Fracture Morphology

Figure 6 illustrates the fracture morphologies of specimens tested at 600 – 1200 °C. At 600 °C (**Figure 6**(a)), the fracture surface exhibits numerous pits of varying sizes and depths, characteristic of typical dimples that are particularly prominent at grain boundaries. This morphology indicates intragranular void formation during deformation, where voids grow and coalesce with increasing strain, leading to necking and eventual transgranular ductile fracture. Within the temperature range of 650 - 1000 °C, as depicted in **Figure 6**(b)-(d), the characteristics of brittle fracture on the fracture surface become more pronounced, exhibiting a granular morphology akin to sugar grains. Additionally, a limited number of dimples are observed on the fracture surface. Consequently, the fracture mode is identified as a combination of ductile fracture and intergranular brittle fracture. As illustrated in **Figure 6**(e)-(h), the fracture surface of the sample exhibits a sugar-like appearance, characteristic of typical brittle fracture. In **Figure 6**(i), the majority of the fracture surface displays the sugar-like appearance, indicative of intergranular brittle fracture. Additionally, a limited number of dendritic structures, resulting from localized melting, are observed on the fracture surface. Within the temperature range of 1050 - 1200 °C, as shown in **Figure 6**(j), due to excessive melting, the fracture surface loses some morphological features, but still retains some large and deep dimples, indicating that ductile fracture has occurred. According to **Figure 6**(k)-(m), the fracture surface shows large and deep dimples, indicating that ductile fracture has occurred.

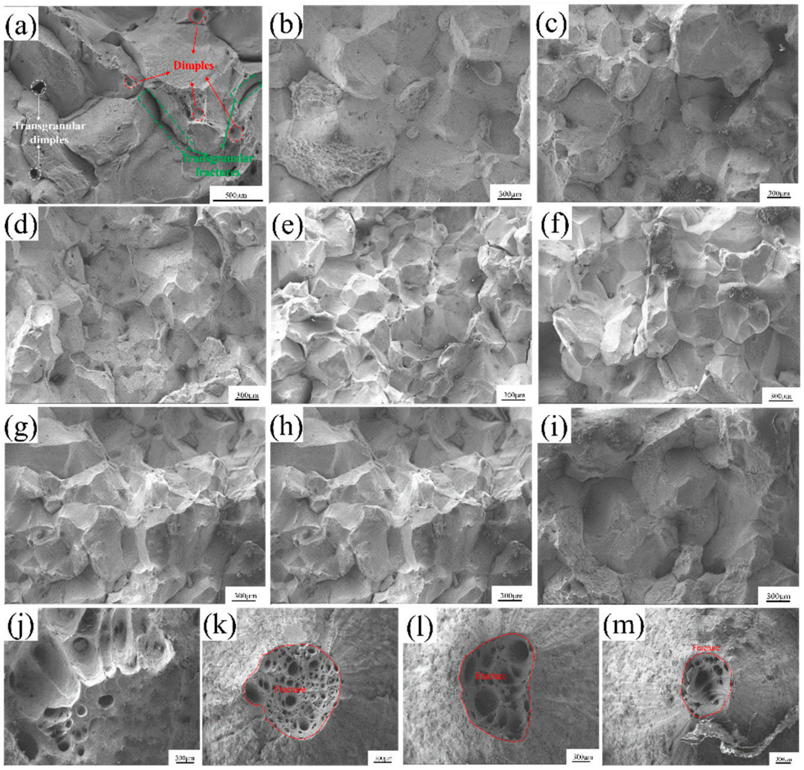

Figure 6. Fracture morphologies of the specimen after hot tensile testing at different temperatures: (a)600 °C; (b)650 °C; (c)700 °C; (d)750 °C; (e)800 °C; (f)850 °C; (g)900 °C; (h)950 °C; (i)1000 °C; (j)1050 °C; (k)1100 °C; (l)1050 °C; (m)1200 °C.

3.4. Microstructure Characterization

Figure 7 shows the microstructure near the tensile fracture of the steel within the test temperature range of 600 - 1200 °C. At 600 °C, the microstructure is widmanstatten. Meanwhile, continuous proeutectoid ferrite precipitates at the grain boundaries and distributes in a network pattern with uneven thickness, with an average thickness of approximately 2 μm, as shown in **Figure 7** (a). At 650 °C and 700 °C, the microstructure is composed of continuous network proeutectoid ferrite precipitated along the grain boundaries, pearlite, and intragranular ferrite. Among them, the thickness of the proeutectoid ferrite is inconsistent, with average thicknesses of 2.2 μm and 3 μm respectively, as shown in **Figure 7**(b) and (c). At 750 °C, the microstructure is composed of continuous network proeutectoid ferrite precipitated along the grain boundaries, martensite, and a small amount of intragranular ferrite, and the average thickness of the proeutectoid ferrite is 3.8 μm, as shown in **Figure 7**(d). At 800 °C, the microstructure consists of the precipitation of proeutectoid ferrite and martensite, and the average thickness of the proeutectoid ferrite is 12 μm, as shown in **Figure 7**(e). At 850 °C, the structure is composed of the precipitation of proeutectoid ferrite and martensite, and the average thickness of the proeutectoid ferrite is 15 μm, as shown in **Figure 7**(f). Within the temperature range of 600 - 850 °C, the proeutectoid ferrite distributes in a network pattern along the grain boundaries, which deteriorates the hot ductility of this steel. Meanwhile, the hot ductility of the specimen decreases with the increase in the average thickness of the proeutectoid ferrite. At 900 - 1200 °C, the microstructure of the specimen is austenite, which transforms into martensite after rapid cooling, as shown in **Figure 7**(g) to (m).

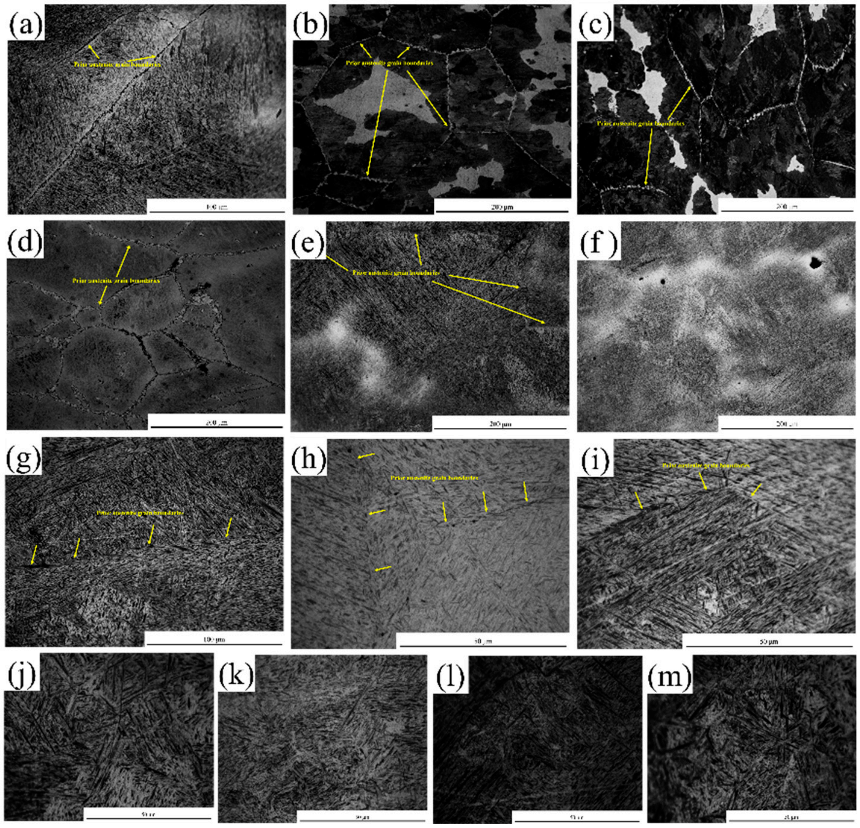

Figure 7. Microstructure near tensile fracture of the steel at different temperatures: (a)600 °C; (b)650 °C; (c)700 °C; (d)750 °C; (e)800 °C; (f)850 °C; (g)900 °C; (h)950 °C; (i)1000 °C; (j)1050 °C; (k)1100 °C; (l)1050 °C; (m)1200 °C.

3.5. Mechanism of Hot Ductility Evolution

Based on the RA values, temperatures of 600 °C, 850 °C, 950 °C, and 1100 °C were selected to investigate the effects of microstructures and precipitated phases on hot ductility.

(i) Precipitate

The characteristics of the phases of the experimental steel (the chemical composition of which is presented in **Table 1**) were calculated by means of Thermo-Calc, as shown in **Figure 8**. Within the temperature range of 400 - 1600 °C, the precipitation characteristics of the liquid phase, austenite (γ), and ferrite (α) in the experimental steel are listed in **Table 2**. As the temperature decreases from 1600 °C to 400 °C, the γ preferentially precipitates from the liquid phase at 1474 °C. When the temperature drops to 870 °C, the γ begins to transform into the α, and at 740 °C, the γ is completely transformed into the α and disappears entirely.

Table 2. Phases characteristics of the experimental steel.

Precipitation	Start precipitating temperature (°C)	Full precipitating temperature (°C)	Maximum precipitation amount (volume fraction)
α	870	-	0.932
γ	1474	740	1
Liquid	-	1444	1

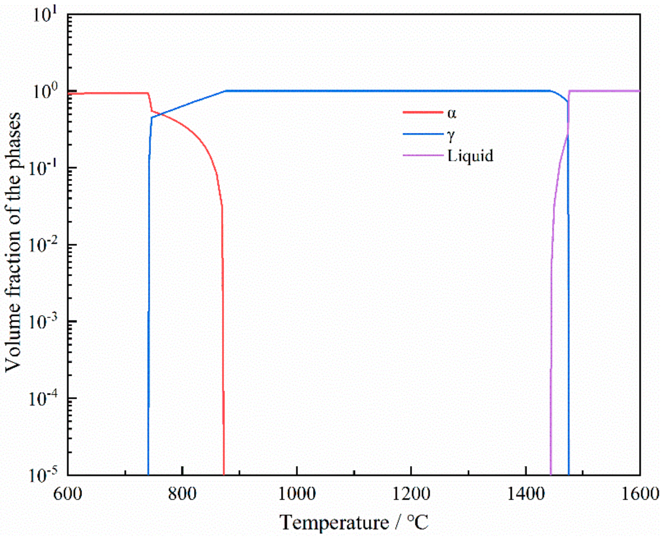

Figure 8. Equilibrium phase behavior in tested steel.

Thermodynamic calculations show that the initial precipitation temperatures of TiC, Ti(C,N), and AlN are 1444 °C, 1380 °C, and 1320 °C, respectively. As the nitrogen content in 38CrMoAl steel is extremely low (~0.0031 wt%), titanium (~0.0127 wt%) preferentially combines with nitrogen at high temperatures *[19,20]*. Therefore, the precipitated phases in the sample are Ti-rich precipitates are Ti(C,N) or TiC. **Figure 9** illustrates the morphologies and compositions of the precipitated phases at 600°C, 850°C, 950°C, and 1100°C, respectively. At 600°C, the precipitates are identified as Ti(C,N) (**Figure 9**(a),(b)), displaying hexagonal or rectangular geometries. At 850°C, the precipitated phase is TiC (**Figure 9**(c)), with a rectangular morphology. At 950°C, the precipitates consist of either Ti(C,N) or TiC (**Figure 9** (d), (e)), both exhibiting rectangular shapes. At 1100°C, the precipitated phase is Ti(C,N) (**Figure 9**(f)) with a rectangular shape.

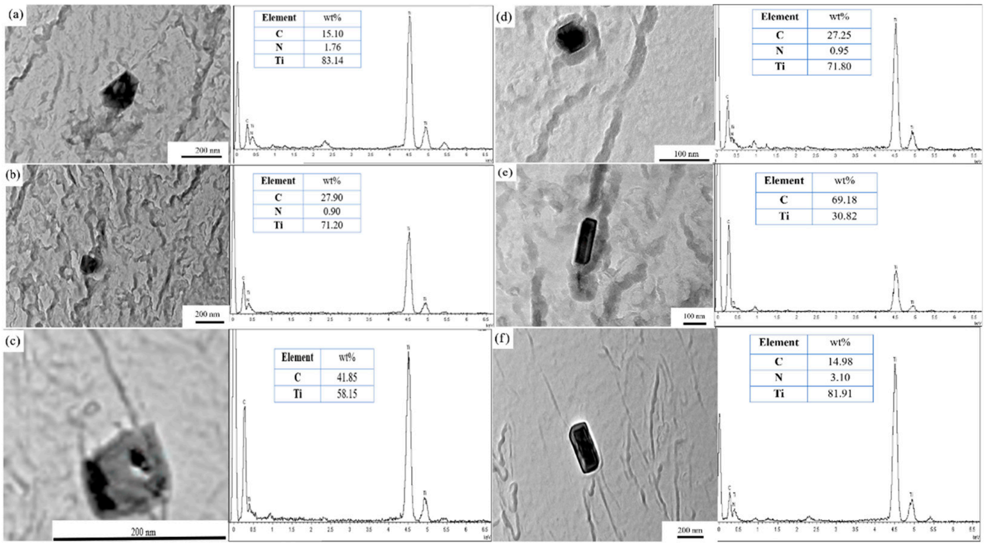

Figure 9. Morphology and composition of precipitates in the tested steels: (a), (b)600 °C; (c)850 °C; (d), (e)950 °C; (f)1100 °C.

Figure 10 presents the variations in the average size and number density of Ti-rich precipitated phases at 600 °C, 850°C, 950 °C, and 1100°C, respectively. As depicted in **Figure 10**(a), the average size of precipitates first decreases, then increases, and finally decreases again. Specifically, the maximum average size of precipitates occurs at 600 °C (~99.37 nm), while the minimum value (~4.39

nm) is observed at 850 °C. According to **Figure 10**(b), the number density of precipitates exhibits an initial increase followed by a decrease, with a peak at 850 °C. The minimum number density is recorded at 600 °C (~1.03 particles/μm²), whereas the maximum value (~47.24 particles/μm²) is attained at 850 °C.

The increase in precipitate quantity and the decrease in precipitate size are detrimental to the hot ductility of steel [30]. The higher the number density of precipitates and the smaller their size, the more pronounced the deterioration of hot ductility [31,32]. Fine precipitation can increase the strength of the matrix, thus intensifying the stress at the boundaries, favoring grain boundary sliding, and when situated at the boundaries can make it easier for intergranular cracks to interlink [31].

During hot tension testing, the deformation mismatch between precipitates and the matrix results in strain concentration. This localized strain can induce significant ductility deformation and promote the nucleation of micro-voids at the precipitates [33]. These micro-voids can act as initiation sites for crack formation, further compromising the hot ductility of the material.

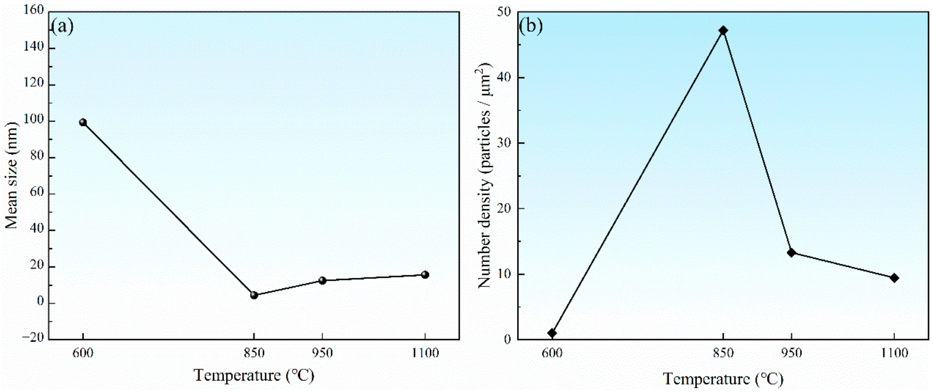

Figure 10. Mean size and number density of precipitates in the tested steels: (a)mean size; (b) number density.

Figure 11 illustrates the mechanism of reduced hot ductility caused by precipitates. Ti-rich precipitates segregate at grain boundaries and form a precipitate free zone (PFZ) around the grain boundaries. Strain tends to concentrate near grain boundaries under stress, primarily because the PFZ exhibits lower hardness [34]. Therefore, as the stress increases, micro-voids form on the grain boundary precipitates. After the voids coalesce, intergranular non-ductile fracture occurs.

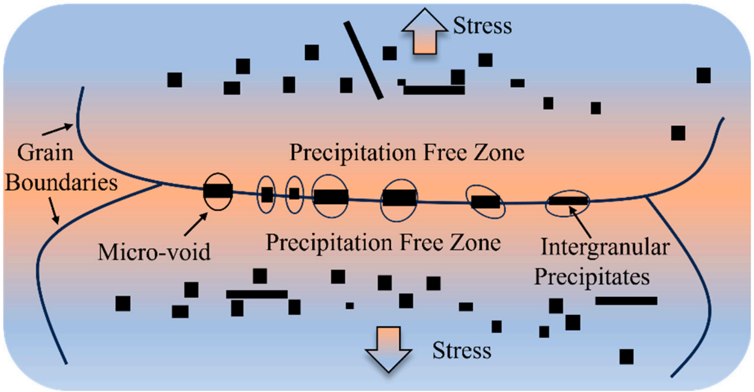

Figure 11. Mechanism of the decrease in hot ductility by precipitates.

Grain sizes adjacent to the fracture surface were quantified using Image-Pro Plus software, with results presented in **Figure 12**. At 600 °C (**Figure 12**(a)), deformed grains exhibit elongation along the tensile axis, accompanied by outward bulging of grain boundaries, indicative of ductility deformation under low-temperature conditions. Coarsening is evident at 850 °C and 950°C (**Figure 12**(b)-(c)), where larger equiaxed grains dominate, likely due to reduced deformation energy and prolonged thermal exposure promoting grain growth. Notably, at 1100 °C (**Figure 12**(d)), coarse deformed grains are replaced by fine dynamic recrystallization (DRX) grains, signaling active grain boundary migration and new grain nucleation under high-temperature conditions. Quantitative analysis (**Figure 12**(e)) reveals a non-monotonic grain size trend: increasing from 600 °C to 850 °C (peak average size ~249.69 μm) before decreasing to ~14.47 μm at 1100 °C. This correlates with the ductility trend, where coarse grains at 850 °C exacerbate intergranular stress concentration (brittle behavior), while fine DRX grains at 1100 °C enhance plastic deformation capacity through improved grain boundary sliding and strain accommodation.

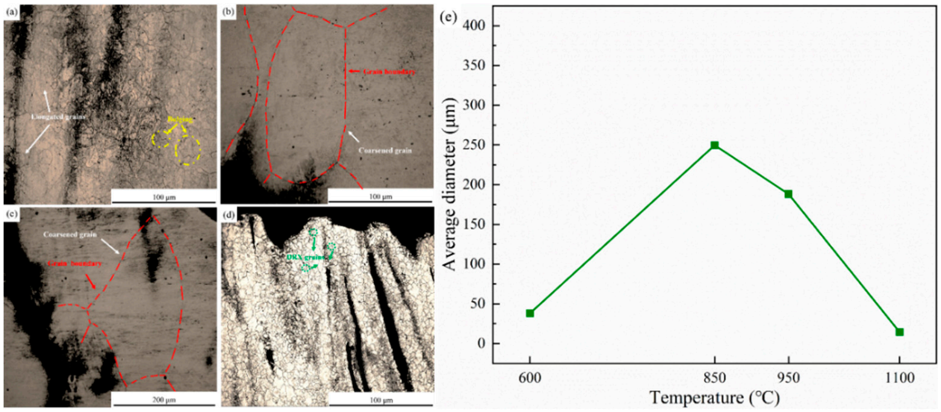

Figure 12. Grain morphology near the fracture surface and average grain size: (a) 600 ℃; (b)850 ℃; (c)950 ℃; (d)1100 ℃; (e)average gain size at 600 ℃, 850 ℃, 950 ℃ and 1100 ℃.

The relationship between precipitate and hot ductility is controlled by their size, number density, and interaction with grain boundaries. The increase in precipitate quantity and the decrease in precipitate size are detrimental to the hot ductility of steel [30]. This mechanism is evident across the four tested temperatures (600 °C, 850 °C, 950 °C, 1100 °C), where precipitate size and density exhibit inverse trends (Figure 10). When the temperature increases from 600 °C to 850 °C, the drastic reduction in precipitate size (from ~ 99.34 nm to ~ 4.40 nm) and simultaneous increase in number density (from ~ 1.03 to ~ 47.24 particles/μm²) enhance precipitate pinning at grain boundaries, theoretically suppressing grain growth. Paradoxically, this regime experiences grain coarsening (from ~122.56 μm to ~249.69 μm), likely due to stress-driven boundary migration under constrained deformation. The fine, dense precipitates act as stress concentrators, promoting intergranular cracking and reducing RA from 57.5% to 26.1%—a classic brittle behavior associated with precipitate-induced grain boundary embrittlement. As the temperature rises from 850 °C to 1100 °C, precipitate coarsening and dissolution at higher temperatures weaken their pinning effect, enabling DRX to dominate. This leads to significant grain refinement (from ~249.69 μm to ~14.47 μm), as DRX nucleates fine grains and eliminates coarse deformed structures. The reduced precipitate density (from ~47.24 to ~3.58 particles/μm²) and grain refinement enhance deformation homogeneity and intergranular coordination, restoring RA values above 40%. These observations are consistent with the results reported in references [35–39].

(ii) Microstructure

The microstructures of the specimens at four different temperatures are shown in **Figure 7**. At 600 °C, the specimen exhibits Widmanstätten with proeutectoid ferrite at grain boundaries, with an average thickness of approximately 2 μm. When the temperature increases to 850 °C, the microstructure consists of martensite and proeutectoid ferrite at grain boundaries, with an average thickness of 15 μm. The strength of intergranular proeutectoid ferrite is generally lower than that of the austenite matrix [40]. During deformation, stress concentrates in these proeutectoid phases, leading to the nucleation, growth, and aggregation of micro-voids at grain boundaries to form cracks, which reduces the hot ductility of steel. The thickness of ferrite at grain boundaries shows a negative correlation with RA values [41]. When straightening stresses exceed the critical strain, cracks initiate along austenite grain boundaries. Consequently, the hot ductility at 600 °C is better than that at 850 °C. As the temperature rises from 850 °C to 950 °C and then to 1100 °C, the microstructure transitions from the $\alpha + \gamma$ two-phase region to a single γ phase (as shown in **Figure 8**). The microstructure of the specimens at 950°C and 1100 °C consists of austenite, which transforms into martensite upon rapid cooling (as shown in **Figure 7**). From 850°C to 950 °C, the proeutectoid ferrite at grain boundaries gradually dissolves into γ phase, causing the microstructure to transition from the $\alpha+\gamma$ two-phase region to a single γ phase. As the temperature rises from 950 °C to 1100 °C and exceeds the critical temperature of the single γ phase region, the microstructure fully transforms into uniform austenite, with its grain size being significantly influenced by temperature. When deformation occurs in the single-phase region above 950 °C, the absence of soft ferrite phase allows stress to be uniformly distributed in the austenite matrix, reducing stress concentration at grain boundaries. As a result, hot ductility is significantly improved compared to the two-phase region (850 °C), with the RA value increasing from 26.1% to over 83.5%.

4. Effect of Heat Treatment on Precipitated Phase and Microstructure

Heat treatment critically regulates precipitated phase evolution and microstructural features in steel, with holding time and cooling rate serving as key determinants *[*42]. Prolonged holding time tends to facilitate the coarsening precipitate and diminish their number density, while rapid cooling suppresses proeutectoid phase formation and induces metastable structures. These modifications directly influence intergranular stress distribution and DRX capacity, thereby governing hot ductility *[43–46*].

Thus, this study investigates the effects of different holding times and cooling rates on the precipitated phases and microstructure of 38CrMoAl steel. The average size and number density of precipitated phases under varying holding times and cooling rates are shown in **Figure 13**.

Figure 13(a) reveals that under three cooling conditions (water cooling, air cooling, furnace cooling), the average size of precipitated phases exhibits a trend of decrease-increase-decrease with increasing holding time: (1) At holding times of 20 min, 80 min, and 100 min, the average size of precipitated phases follows the order: furnace cooling > air cooling > water cooling; (2) At holding times of 40 min and 60 min, the order changes to: furnace cooling > water cooling > air cooling. **Figure 13**(b) shows that the variation trend of precipitate number density is inverse to that of average size: (1) At holding times of 20 min, 80 min, and 100 min, the number density order is: water cooling > air cooling > furnace cooling; (2) At holding times of 40 min and 60 min, the order becomes: air cooling > water cooling > furnace cooling.

Water cooling inhibits precipitate coarsening and promotes the formation of fine precipitates with high number density, which is particularly obvious at holding of 20 min, 80 min and 100 min. This is because the rapid cooling rate associated with water quenching reduces the average size of precipitates and enhances their nucleation rate *[*47]. In contrast, furnace cooling prolongs atomic diffusion, leading to precipitate coarsening and a decrease in number density. At moderate holding of 40min and 60 min, under air cooling, the competition between dynamic recrystallization and precipitate formation may generate a unique size distribution of precipitates. This is due to the interplay between the driving force for recrystallization and the pinning force of precipitates, which can lead to a more complex microstructural evolution *[*48].

The reduction in precipitate average size and the increase in number density are detrimental to hot ductility. under the same holding time conditions, decreasing the cooling rate can promote the coarsening of precipitate size and the reduction in number density, which is beneficial to the hot ductility of the specimen. In contrast, a higher cooling rate results in finer precipitates with a higher number density, which can impair hot ductility.

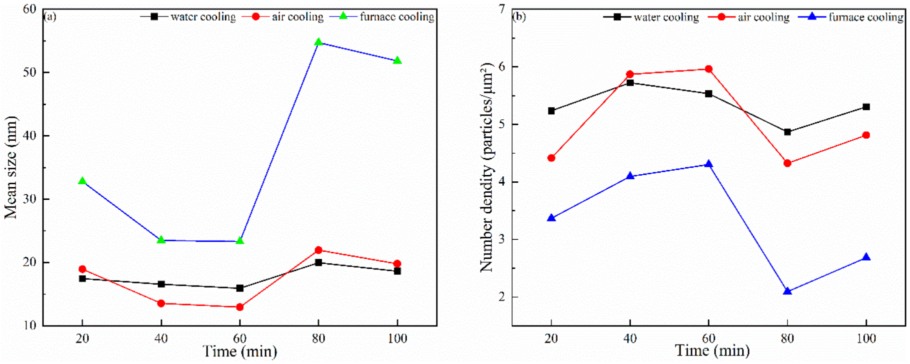

Figure 13. Average size and number density of precipitated phases under different holding times and cooling rates: (a)mean size; (b) number density.

Figure 14 illustrates the microstructural transformations in 38CrMoAl steel under different combinations of holding time and cooling rate. At a constant holding time, increasing the cooling rate (furnace cooling → air cooling → water cooling) drives the following phase transitions: ferrite → bainite + ferrite → martensite + proeutectoid ferrite.

It can be seen from **Figure 14**(a1) ~ (a5) that as the holding time increases from 20 min to 100 min, the thickness of proeutectoid ferrite precipitated along the grain boundaries exhibits a sequential trend of increasing, decreasing, and then increasing. As observed in **Figure 14**(b1) ~ (b5), the area fraction of ferrite increases with the prolongation of holding time. Under furnace cooling conditions, the microstructure consists of ferrite, as shown in the **Figure 14**(c1) ~ (c5).

The hot ductility of steel is significantly influenced by its microstructure. When martensite and proeutectoid ferrite coexist in steel, martensite exhibits high hardness and poor ductility; a higher content of martensite will reduce the overall ductility of steel. If proeutectoid ferrite distributes along grain boundaries in a coarse network morphology, it will disrupt the matrix continuity, weaken grain boundary bonding, and deteriorate hot ductility. When bainite and ferrite coexist, lower bainite can improve the hot ductility of steel due to its superior comprehensive mechanical properties. Ferrite itself has good ductility and toughness, and a higher proportion of ferrite helps enhance the deformation capacity of steel during hot ductility. For example, the steel grade studied in Reference *[49,50*] forms a bainite + ferrite microstructure under specific cooling conditions, demonstrating excellent hot ductility characteristics. Ferrite has a significant impact on the hot ductility of steel, with its content, morphology, and distribution being crucial. Generally, uniform and fine ferrite microstructures can improve hot ductility.

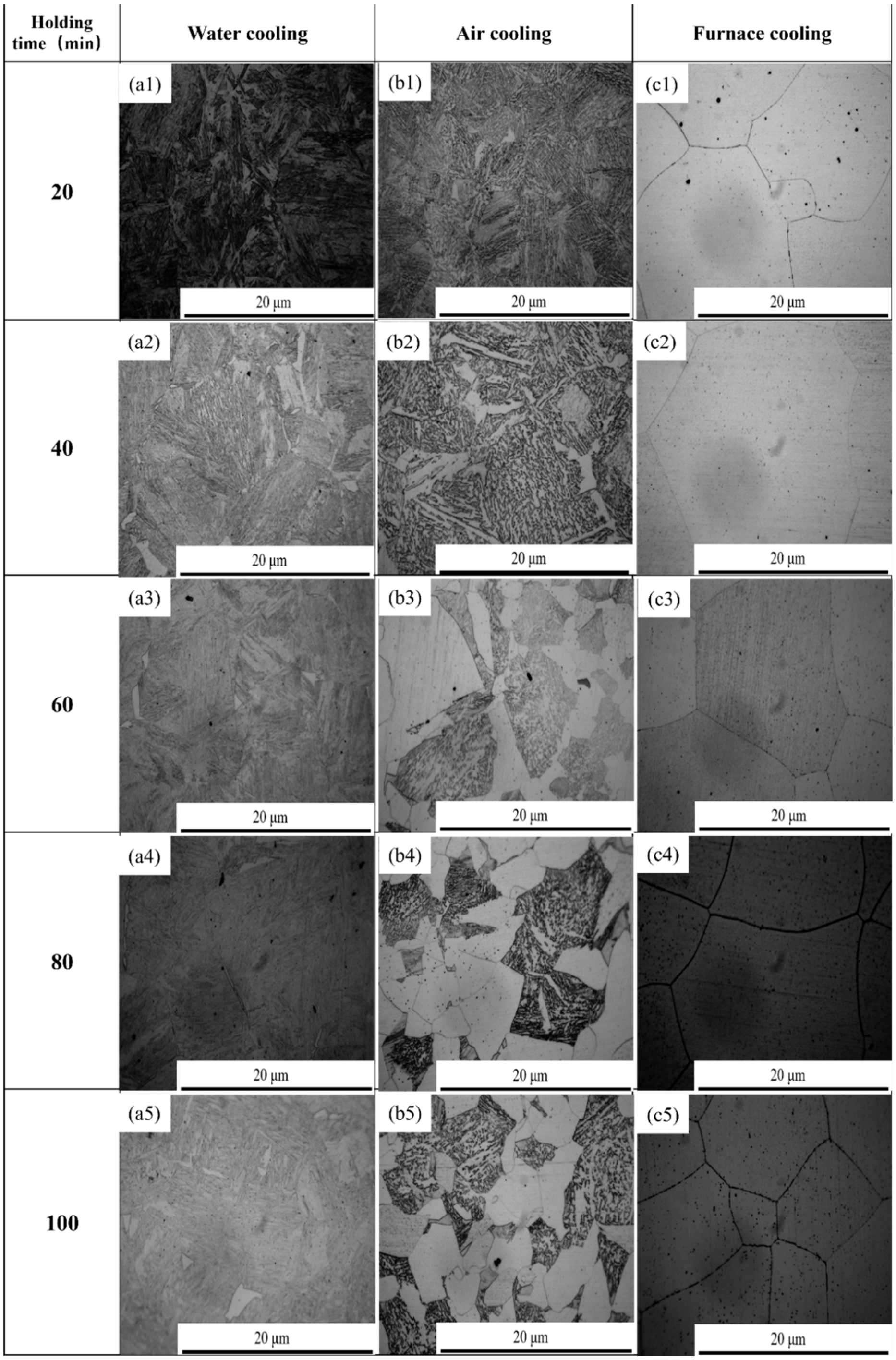

Figure 14. Microstructure of 38CrMoAl steel under different holding times and cooling rates: (a1) ~ (a5) holding time for 20 to 100 minutes at water cooling; (b1) ~ (b5) holding time for 20 to 100 minutes at air cooling; (c1) ~ (c5) holding time for 20 to 100 minutes at furnace cooling.

Martensite, a hard and brittle phase with a hardness of 400 - 600 HV, exhibits a lath or acicular morphology, contributing to localized stress concentration due to its low ductility. The formation of proeutectoid ferrite networks along grain boundaries disrupts matrix continuity, creating preferential paths for crack initiation during deformation. In contrast, bainite (hardness: 300 - 450 HV), characterized by needle-like or lath-shaped structures, forms a "soft-hard alternating" composite with ferrite (hardness: ~150 - 200 HV). This heterogeneous structure balances strength and ductility, as the softer ferrite phase (predominantly in blocky or acicular forms with uniform distribution) facilitates plastic deformation, while bainite provides load-bearing capacity. Single-phase ferrite microstructures, with their uniform deformation behavior and low resistance to grain boundary sliding, significantly reduce crack susceptibility. For 38CrMoAl steel, decreasing the cooling rate under constant holding time conditions promotes the formation of coarse ferrite and bainite-ferrite mixtures rather than brittle martensite, thereby enhancing hot ductility through improved intergranular cohesion and deformation homogeneity.

5. Conclusion

To address the issue of casting slab cracking, this study investigates the high-temperature mechanical properties of 38CrMoAl steel to determine the brittle temperature range prone to cracking and the fracture type, analyze the causes of poor hot ductility in each temperature range, and conducts research on the heat treatment of 38CrMoAl steel. The main conclusions are as follows:

(1) The high-temperature tensile test of 38CrMoAl steel was carried out using Gleeble-3800. Based on the criterion of RA = 40%, the steel does not exhibit the first and second brittle zones, and the temperature range of the third brittle zone is 645 -1009 °C, straightening or processing within the brittle zone temperature range of the casting slabs should be avoided as much as possible.

(2) From the fracture morphology, it can be seen that the specimens exhibit ductile fracture in the temperature ranges of 600 °C and 1050 - 1200 °C. In the temperature range of 650 - 750 °C, the specimens show a combination of ductile fracture and intergranular brittle fracture. Within the temperature range of 800 - 1000 °C, the specimens undergo intergranular brittle fracture.

(3) The fracture mechanisms of 38CrMoAl steel are classified into three types:(I)In the α single-phase region, the thickness of intergranular proeutectoid ferrite increases with rising temperature, reducing hot ductility;(II)In the γ single-phase region, the average size of precipitates increases and the number density decreases with increasing temperature, improving hot ductility;(III)In the $\alpha + \gamma$ two-phase region, the precipitation of proeutectoid ferrite facilitates crack propagation, and the dense distribution of precipitates at grain boundaries causes stress concentration, deteriorating hot ductility.

(4) The analysis of heat treatment for 38CrMoAl steel shows that with the same holding time, the microstructure of the specimen transforms as the cooling rate increases: ferrite → bainite + ferrite → martensite + proeutectoid ferrite; Under three cooling conditions (water cooling, air cooling, and furnace cooling), the average size of precipitates exhibits a trend of decreasing first, then increasing, and decreasing again with the increase in holding time:(I) At holding times of 20 min, 80 min, and 100 min, the average sizes of precipitates follow the order: furnace cooling > air cooling > water cooling;(II) At holding times of 40 min and 60 min, the order changes to: furnace cooling > water cooling > air cooling. The variation trend of precipitate number density is opposite to that of average size.

Author Contributions: Bo Song and Wei Liu conceived the work. Guofang Xu performed the experiments and analyzed the data. Guofang Xu and Wei Liu wrote the manuscript with help from all the other authors. All authors supervise the whole project and have read and agreed to the published version of the manuscript.

Acknowledgments: The present work was supported by the Wuhu Xinxing Ductile Pipe Co., Ltd., China.

Funding: No.

Data Availability Statement: The data presented in this study are available on request from the corresponding author. The data are not publicly available due to involving trade secrets.

Conflicts of Interest: The authors declare no conflict of interest.

References

1. Steels, GB/T 3077-2015. Beijing: STANDARD PRESS OF CHINA; 2016.
2. Ren X, Wang R, Wei D, Huang Y, Zhang H. Study on surface alloying of 38CrMoAl steel by electron beam. Nucl. Instrum. Methods Phys Res Sect. B 2021;505: 44-49. https://doi.org/10.1016/j.nimb.2021.08.005.

3. Chen Y, Song L, Zhang C, Ye X, Song R, Wang Z et al. Plasma nitriding without formation of compound layer for 38CrMoAl hydraulic plunger. Vacuum 2017;143: 98-101. https://doi.org/10.1016/j.vacuum.2017.05.036.
4. Zhang Z, Mao H, Chen Y, Wu X, Zhou S, Hu W. Dynamic fracture toughness and damage mechanism of 38CrMoAl steel under salt spray corrosion. Theor Appl Fract Mech 2022;119: 103382. https://doi.org/10.1016/j.tafmec.2022.103382.
5. Tan R, Liu W, Song B, Yang S, Chen Y, Zuo X et al. Numerical simulation on solidification behavior and structure of 38CrMoAl large round bloom using CAFE model. J Iron Steel Res Int 2023;30: 1222-1233. https://doi.org/10.1007/s42243-023-00972-y.
6. Steenken B, Rezende JLL, Senk D. Hot ductility behaviour of high manganese steels with varying aluminium contents. Mater Sci Technol 2017;33: 567-573. https://doi.org/10.1080/02670836.2016.1235855.
7. Ba L, Di X, Li C, Pan J, Ma C, Qu Y et al. Enhancing hot ductility of a cryogenic high manganese steel at a high strain rate by matrix homogenization. Mater Sci Eng A 2023;872: 145002. https://doi.org/10.1016/j.msea.2023.145002.
8. Kang SE, Kang MH, Mintz B. Influence of vanadium, boron and titanium on hot ductility of high al, TWIP steels. Mater Sci Technol 2021;37: 42-58. https://doi.org/10.1080/02670836.2020.1861736.
9. Kang SE, Banerjee JR, Mintz B. Influence of s and AlN on hot ductility of high al, TWIP steels. Mater Sci Technol 2012;28: 589-596. https://doi.org/10.1179/1743284711Y.0000000109.
10. Kang SE, Tuling A, Lau I, Banerjee JR, Mintz B. The hot ductility of Nb/V containing high al, TWIP steels. Mater Sci Technol 2011;27: 909-915. https://doi.org/10.1179/026708309X12595712305915.
11. Trang TTT, Lee S, Heo Y, Kang M, Lee D, Lee JS et al. Improved hot ductility of an as-cast high Mn TWIP steel by direct implementation of an MnS-containing master alloy. Scr Mater 2022;215: 114685. https://doi.org/10.1016/j.scriptamat.2022.114685.
12. Calvo J, Cabrera JM, Rezaeian A, Yue S. Evaluation of the hot ductility of a C–Mn steel produced from scrap recycling. ISIJ Int 2007;47: 1518-1526. https://doi.org/10.2355/isijinternational.47.1518.
13. Wang Y, Zhao S, Song R, Hu B. Hot ductility behavior of a Fe-0.3C-9Mn-2Al medium Mn steel. Int J Miner Metall Mater 2021;28: 422-429. https://doi.org/10.1007/s12613-020-2206-x.
14. Hassan MM, Shafiq MA, Mourad SA. Experimental study on cracked steel plates with different damage levels strengthened by CFRP laminates. Int J Fatigue 2021;142: 105914. https://doi.org/10.1016/j.ijfatigue.2020.105914.
15. Bhattacharya D, Roy TK, Mahashabde VV. A study to establish correlation between intercolumnar cracks in slabs and off-center defects in hot-rolled products. J Fail Anal Prev 2016;16: 95-103. https://doi.org/10.1007/s11668-015-0050-5.
16. Zhang M, Bao Y, Zhao L, Chen J, Zheng H. Formation and control of central cracks in alloy steel ZKG223. Steel Res Int 2022;93. https://doi.org/10.1002/srin.202200289.
17. Wang Y, Yang J, Wang R, Xin X, Xu L. Effects of non-metallic inclusions on hot ductility of high manganese TWIP steels containing different aluminum contents. Metall Mater Trans B-Proc Metall Mater Proc Sci 2016;47: 1697-1712. https://doi.org/10.1007/s11663-016-0626-9.
18. Wang Y. Solidification structure, non-metallic inclusions and hot ductility of continuously cast high manganese TWIP steel slab. ISIJ Int 2019;59: 872-879.
19. https://doi.org/10.2355/isijinternational.ISIJINT-2018-694.
20. Borrmann L, Senk D, Steenken B, Rezende JLL. Influence of cooling and strain rates on the hot ductility of high manganese steels within the system Fe–Mn–Al–C. Steel Res Int 2021;92: 2000346. https://doi.org/10.1002/srin.202000346.
21. Qaban A, Mintz B, Kang SE, Naher S. Hot ductility of high Al TWIP steels containing Nb and Nb-V. Mater Sci Technol 2017;33: 1645-1656. https://doi.org/10.1080/02670836.2017.1309097.
22. Kang SE, Banerjee JR, Tuling A, Mintz B. Influence of P and N on hot ductility of high Al, boron containing TWIP steels. Mater Sci Technol 2014;30: 1328-1335. https://doi.org/10.1179/1743284714Y.0000000576.
23. Vedani M, Dellasega D, Mannuccii A. Characterization of grain-boundary precipitates after hot-ductility tests of microalloyed steels. ISIJ Int 2009;49: 446-452. https://doi.org/10.2355/isijinternational.49.446.

24. Qian G, Cheng G, Hou Z. Effect of the induced ferrite and precipitates of Nb–Ti bearing steel on the ductility of continuous casting slab. ISIJ Int 2014;54: 1611-1620. https://doi.org/10.2355/isijinternational.54.1611.
25. Cheng Z, Liu J, Wu R, Liu G, Wang S. Effect of V on the hot ductility behavior of high-strength hot-stamped steels and associated microstructural features. Metall Mater Trans a Phys Metall Mater Sci 2023;54: 3476-3488. https://doi.org/10.1007/s11661-023-07083-z.
26. Chen XM, Song SH, Sun ZC, Liu SJ, Weng LQ, Yuan ZX. Effect of microstructural features on the hot ductility of 2.25Cr–1Mo steel. Mater Sci Eng A 2010;527: 2725-2732. https://doi.org/10.1016/j.msea.2010.01.047.
27. Sun Z, Shen D, Liu G, Guo N, Guo F, Zhang Z et al. Influence of microstructure evolution on hot ductility behavior of a Cr and Mo alloyed Fe-C-Mn steel during hot deformation. Mater Today Commun 2024;39: 109164. https://doi.org/10.1016/j.mtcomm.2024.109164.
28. Tuling A, Banerjee JR, Mintz B. Influence of peritectic phase transformation on hot ductility of high aluminium TRIP steels containing Nb. Mater Sci Technol 2011;27: 1724-1731. https://doi.org/10.1179/1743284711Y.0000000013.
29. Tacikowski M, Osinkolu GA, Kobylanski A. Segregation-induced intergranular brittleness of ultrahigh-purity Fe–S alloys. Mater Sci Technol 1986;2: 154-158. https://doi.org/10.1179/mst.1986.2.2.154.
30. Mejía I, Altamirano G, Bedolla-Jacuinde A, Cabrera JM. Effect of boron on the hot ductility behavior of a low carbon advanced ultra-high strength steel (a-UHSS). Metall Mater Trans a Phys Metall Mater Sci 2013;44: 5165-5176. https://doi.org/10.1007/s11661-013-1870-0.
31. Kizu T, Urabe T. Hot ductility of sulfur-containing low manganese mild steels at high strain rate. ISIJ Int 2009;49: 1424-1431. https://doi.org/10.2355/isijinternational.49.1424.
32. Spradbery C, Mintz B. Influence of undercooling thermal cycle on hot ductility of C-Mn-Al-Ti and C-Mn-Al-Nb-Ti steels. Ironmak Steelmak 2005;32: 319-324. https://doi.org/10.1179/174328105X48016.
33. Banks K, Koursaris A, Verdoorn F, Tuling A. Precipitation and hot ductility of low C-V and low C-V-Nb microalloyed steels during thin slab casting. Mater Sci Technol 2001;17: 1596-1604. https://doi.org/10.1179/026708301101509665.
34. Mejía I, Salas-Reyes AE, Calvo J, Cabrera JM. Effect of Ti and B microadditions on the hot ductility behavior of a high-Mn austenitic Fe–23Mn–1.5Al–1.3Si–0.5C TWIP steel. Mater Sci Eng A 2015;648: 311-329.
35. https://doi.org/10.1016/j.msea.2015.09.079.
36. Hornbogen E, Graf M. Fracture toughness of precipitation hardened alloys containing narrow soft zones at grain boundaries. Acta Metallurgica 1977;25: 877-881. https:/doi.org/10.1016/0001-6160(77)90173-0.
37. Li J, Jiang B, Zhang C, Zhou L, Liu Y. Hot embrittlement and effect of grain size on hot ductility of martensitic heat-resistant steels. Mater Sci Eng A 2016;677: 274-280. https://doi.org/10.1016/j.msea.2016.09.072.
38. Cai Z, An J, Cheng B, Zhu M. Effect of austenite grain size on the hot ductility of nb-bearing peritectic steel. Metall Mater Trans a Phys Metall Mater Sci 2023;54: 141-152. https://doi.org/10.1007/s11661-022-06854-4.
39. Furumai K, Wang X, Zurob H, Phillion A. Evaluating the effect of the competition between NbC precipitation and grain size evolution on the hot ductility of nb containing steels. ISIJ Int 2019;59: 1064-1071. https://doi.org/10.2355/isijinternational.ISIJINT-2018-716.
40. Wang Z, Wang Y, Wang C. Grain size effect on the hot ductility of high-nitrogen austenitic stainless steel in the presence of precipitates. Materials (Basel) 2018;11: 1026. https://doi.org/10.3390/ma11061026.
41. Mintz B, Kang S, Qaban A. The influence of grain size and precipitation and a boron addition on the hot ductility of a high Al, V containing TWIP steels. Mater Sci Technol 2021;37: 1035-1046. https://doi.org/10.1080/02670836.2021.1975876.
42. Liu Y, Sun Y, Wu H. Effects of chromium on the microstructure and hot ductility of Nb-microalloyed steel. Int J Miner Metall Mater 2021;28: 1011-1021. https://doi.org/10.1007/s12613-020-2092-2.
43. Yang X, Zhang L, Li S, Li M. Influence of cooling conditions on the hot ductility of Nb-Ti-bearing steels. Metall Res Technol 2015;112: 604. https://doi.org/10.1051/metal/2015038.

44. Qayyum F, Darabi AC, Guk S, Guski V, Schmauder S, Prahl U. Analyzing the effects of Cr and Mo on the pearlite formation in hypereutectoid steel using experiments and phase field numerical simulations. Materials (Basel) 2024;17: 3538. https://doi.org/10.3390/ma17143538.
45. Jia Z, Zhang Y, Meng F, Yu Q, Sun F, Sun H et al. Improving the uniform deformation ability and ductility of powder metallurgical Ti2AlNb intermetallic with single-step solution heat treatment. J Alloys Compd 2025;1011: 178377. https://doi.org/10.1016/j.jallcom.2024.178377.
46. Jin Y, Zhou W. Hot ductility loss and recovery in the CGHAZ of T23 steel during post-weld heat treatment at 750 °C. ISIJ Int 2017;57: 517-523. https://doi.org/10.2355/isijinternational.ISIJINT-2016-594.
47. Qu HP, Lang YP, Yao CF, Chen HT, Yang CQ. The effect of heat treatment on recrystallized microstructure, precipitation and ductility of hot-rolled Fe–Cr–Al–REM ferritic stainless steel sheets. Mater Sci Eng A 2013;562: 9-16. https://doi.org/10.1016/j.msea.2012.11.008.
48. Andersson J, Sjöberg GP, Viskari L, Chaturvedi M. Effect of different solution heat treatments on hot ductility of superalloys Part 2 – Allvac 718Plus. Mater Sci Technol 2012;28: 733-741. https://doi.org/10.1179/1743284712Y.0000000002.
49. Fu J, Du W, Jia L, Wang Y, Zhu X, Du X. Cooling rate controlled basal precipitates and age hardening response of solid-soluted Mg–Gd–Er–Zn–Zr alloy. J Magnes Alloy 2021;9: 1261-1271. https://doi.org/10.1016/j.jma.2020.06.014.
50. Chen S, Li L, Xia J, Peng Z, Gao J, Sun H. Recrystallization-precipitation interaction of a Ti microalloyed steel with controlled rolling process. J Phys Conf Ser 2020;1676: 12036. https://doi.org/10.1088/1742-6596/1676/1/012036.
51. Jiang B, Hu X, Zhou L, Wang H, Liu Y, Gou F. Effect of transformation temperature on the ferrite–bainite microstructures, mechanical properties and the deformation behavior in a hot-rolled dual phase steel. Met Mater-Int 2021;27: 319-327. https://doi.org/10.1007/s12540-019-00371-7.
50. Dongxin Y, Yuman Q, Zhao D, Xiaoyan L, Fucheng Z, Zhinan Y et al. Investigating microstructural properties of ferrite/bainite dual-phase steel through simple process control. Mater Sci Technol 2022;38: 1348-1357. https://doi.org/10.1080/02670836.2022.2078934.